International Journal on Interactive Design and Manufacturing (IJIDeM)
https://doi.org/10.1007/s12008-025-02390-8

ORIGINAL ARTICLE

Influence of geometry and printing parameters on the dimensional and geometrical accuracy of 316L binder jetting green product

Marco Zago[1] · **Matteo Perina**[2] · **Ilaria Cristofolini**[1]

Received: 25 February 2025 / Revised: 5 August 2025 / Accepted: 11 August 2025

Abstract

Metal Binder Jetting (MBJ) has a great potential for producing complex products in medium to large batches. However, challenges remain in achieving high dimensional and geometrical accuracy. This study investigates the influence of printing parameters and sample geometry on the accuracy of 316L stainless steel green products produced via MBJ. A Design of Experiments (DoE) approach was employed to study four factors at three levels. A Taguchi L9 orthogonal array was designed to evaluate the effects of printhead speed, binder saturation grade, blade speed, and shell thickness on dimensional and geometrical accuracy. Four different geometries were printed and then measured using a coordinate measuring machine (CMM) to assess the accuracy of external and internal dimensions, flatness, and parallelism. The results showed that dimensional accuracy was influenced by printing direction, feature size, and the feature type. External dimensions showed highest accuracy along the powder spreading direction (Y: 0.12% ± 0.21%), followed by building direction (Z: 0.25% ± 0.3%) and binder injection direction (X: 0.40% ± 0.2%). Significantly lower accuracy was found in internal features, showing a negative deviation (X: − 0.66% ± 0.32%; Y: − 0.41% ± 0.23%).

Flatness and parallelism errors were found almost constant across experiments, with average values of 0.014 ± 0.008 and 0.024 ± 0.014, respectively. Parallelism appeared to be affected by geometry, specifically, increasing height-to-thickness ratios led to larger errors. Grey relational analysis identified printhead speed as the most critical parameter, followed by binder saturation grade, shell thickness, and blade speed in optimizing the accuracy of the printed parts. ANOVA analysis reveals that printhead has a statistical relevance showing a P-value of 0.029. This work provides novel insights into the printing factors affecting the quality of green parts produced by MBJ. This article helps in identifying the optimal printing parameters for binder jetting of SS 316L.

✉ Marco Zago
marco.zago-1@unitn.it

[1] Department of Industrial Engineering, University of Trento, Via Sommarive 9, 38123 Trento, Italy

[2] Mimest S.R.L, Via del Lavoro 30, 38063 Avio, Italy

Published online: 02 September 2025

Graphical abstract

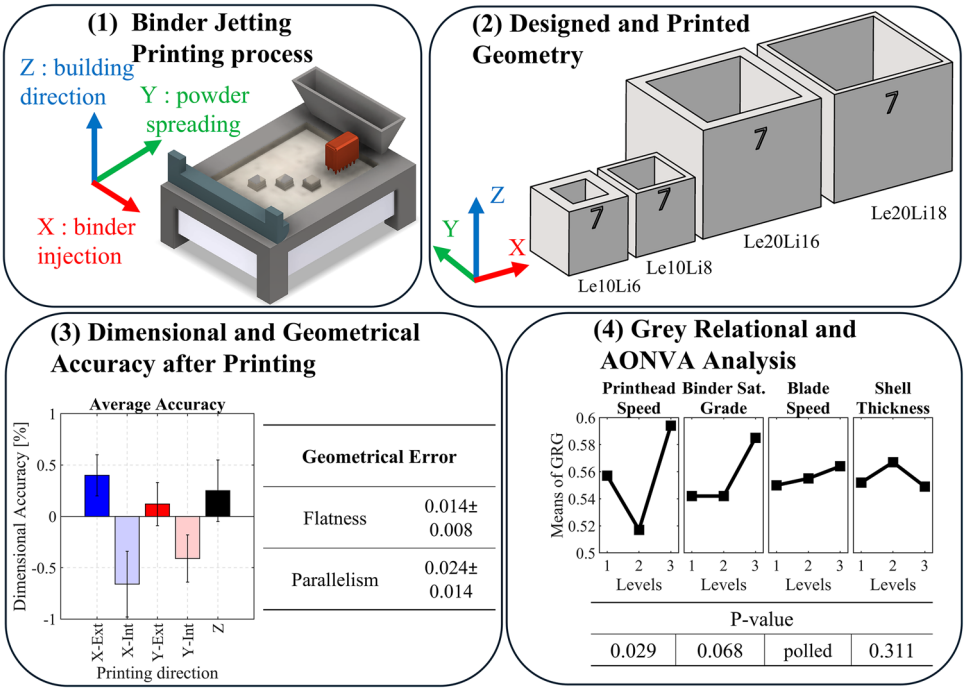

Keywords Design for additive manufacturing · Metal binder jetting · Dimensional accuracy · Geometrical accuracy · Grey relational analysis

1 Introduction

The interest in Additive Manufacturing technologies is continuously growing, thanks to the possibility of producing complex geometries with negligible waste of material, and consequent cost reduction [1]. However, the peculiarities of such technologies determine specific part properties, and potentially specific defects, to be carefully considered [2]. Among the different Additive Manufacturing technologies classified by ISO/ASTM52900:2021, different maturity levels can be recognized; while Fused Deposition Modeling (FDM) and Laser Powder Bed Fusion (LPBF) technologies are well established, other processes as Metal Binder Jetting (MBJ) need for further investigation to fully exploit the strong potential for manufacturing small-medium batches in different fields—consumer goods, medical, automotive, aviation, and aerospace.

Two main steps determine the characteristics of MBJ parts: printing (also comprehending drying, curing, and depowdering) and sintering (also comprehending de-binding). Both of these steps concur to determine the difficulties in controlling product accuracy, in turn currently limiting the widespread adoption of MBJ. Product quality is negatively affected by the anisotropic shrinkage and shape distortion occurring on sintering, but the geometrical inaccuracy also derives from printing, and cannot be amended on sintering.

The strong effect of printing parameters on micro and macro geometrical accuracy has been recognized by literature studies. Surface quality is affected by layer thickness, as expected, and lower roughness is related to thinner layer thickness, as observed by Chen and Zhao on 420 stainless steel parts [3]. Similarly, low roughness can be obtained using powders with small particle size [4]. Binder saturation grade, related to the amount of binder interacting with powder surface, also strongly affects surface quality. Lores et al. [5] reported that poor surface quality can be related to low saturation level, meaning that the amount of deposited binder was not enough to properly bind the powder particles, thus determining particles separation or detachment. On the other hand, high binder saturation grade, meaning excessive amount of deposited binder, and consequently of powder particles bonded to the surface, might also negatively affect surface quality.

Geometrical accuracy is generally ascribed to the dimensional and geometrical variations occurring on sintering, meaning sintering temperature, time, and atmosphere [6–8]. However, shrinkage and its anisotropy are strongly influenced by printing parameters. The staircase effect related to

layer thickness originates geometrical form errors, as analytically quantified in [9] and [10] for flatness and cylindricity, respectively. Indeed, the staircase effect is not the only reason for geometrical inaccuracy, as demonstrated by Zago et al. after measuring flatness [11] and cylindricity [12] of binder jetting products at green and sintered state. As observed for surface quality, binder saturation grade and printing speed [13] have to be carefully tuned to avoid geometrical defects, such as bleeding [14], and layer shifting [11, 15]. Binder drying and curing may also determine a dimensional deviation. Layer shifting may occur when heating temperature is too high and/or drying time is too long, due to the overcure of binder, resulting in weak bonding between layers. Conversely, sticking to the roller may occur when temperature is too low and/or time too short, and poorly cured binder would also result in insufficiently bonded layers [5]. In both cases, detrimentally affecting the accuracy of parts, also implying anisotropic shrinkage [3]. Moreover, depending on the type of binder, drying is often not sufficient to complete water/solvent evaporation and polymer curing, and specific curing in oven at low temperature is generally needed after de-powdering. Effective powder spreading, in turn affected by powder characteristics [16, 17], can be controlled by powder applicator speed to avoid inhomogeneous distribution, and consequently not uniform shrinkage. Finally, inhomogeneities and geometrical inaccuracies may also derive from the position in building chamber [18].

The many issues shortly presented above highlight the difficult task of controlling dimensional and geometrical accuracy in Metal Binder Jetting, due to many different process variables.

This work aims at studying the influence of process parameters on dimensional and geometrical accuracy in squared parts with a through hole made by SS 316L. Taguchi model was adopted to investigate the contribution of four parameters: printhead speed, binder saturation grade, powder applicator speed and shell thickness.

2 Materials and methods

A cubic geometry with a square through-hole was designed for this study. To examine the influence of cube dimensions, four configurations were developed, as illustrated in Fig. 1. The dimensions in the green state are presented in Table 1, they were derived by scaling the expected sintered dimensions to account for anisotropic dimensional changes during sintering.

The build box was organized to include multiple replicates of the four geometries. Samples were positioned at various locations along X, Y, and Z axes, which correspond to:

- X-axis: the direction of printhead injection.

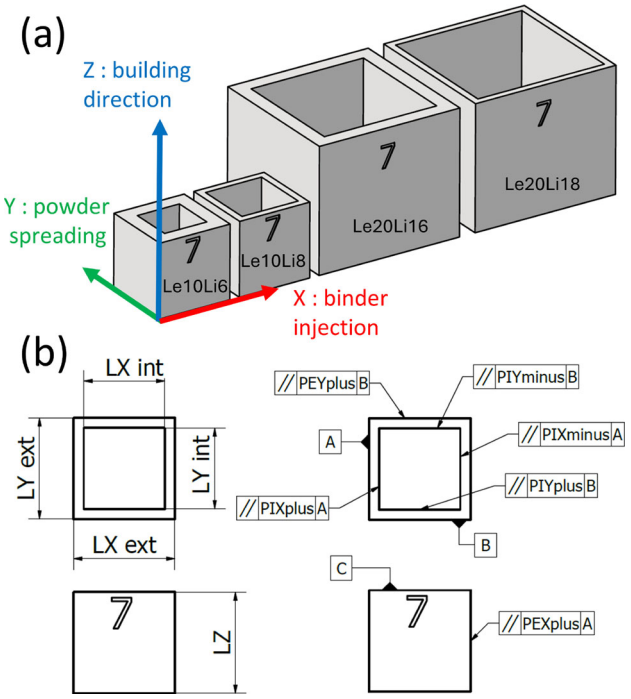

Fig. 1 (**a**) Axonometric view of the four geometries (from left to right: Le10Li6, Le10Li8, Le20Li16, Le20Li18) and (**b**) annotation convention for dimension and parallelism control

- Y-axis: the blade's movement direction (powder spreading).
- Z-axis: the building direction.

A total of 36 replicates each of the Le10Li6 and Le10Li8 geometries were distributed across three build heights, representing different distances from the build plate. Additionally, 9 replicates each of the Le20Li16 and Le20Li18 geometries were distributed at the same three build heights. All samples were aligned with the reference system shown in Fig. 1, and markers were added to facilitate sample identification after printing operations.

The printing process was performed using a Digital Metal® DMP 2000 binder jetting industrial machine with AISI 316L stainless steel powder supplied by Digital Metals (Sweden), now Markforged (USA).

A design of experiments (DoE) approach was implemented to evaluate the effects of printing parameters on the quality of green products. Taguchi's method was applied using an L9 orthogonal array to investigate four factors at three levels. This reduced the number of experiments required from 81 (full factorial design) to 9. A full factorial design offers exhaustive insight into parameter interactions; however, it would demand several weeks of continuous printing and measurement. While Taguchi's L9 orthogonal array provided first order interaction results of the four factors at three levels in just nine runs. For this reason, L9 Taguchi's

Table 1 Nominal dimensions in the green state of the four geometries. For dimension annotations see Fig. 1

Geometry	LX-EXT [mm]	LY-EXT [mm]	LZ [mm]	LX-INT [mm]	LY-INT [mm]
Le10Li6	11.997	12.071	12.177	7.199	7.243
Le10Li8	11.997	12.071	12.177	9.597	9.657
L20Li16	23.994	24.142	20.700	19.196	19.314
Le20Li18	23.994	24.142	20.700	21.594	21.728

method is chosen as an optimal compromise to achieve significant results with a reasonable time. The four printing parameters studied were:

- Printhead speed: The velocity at which the printhead injects binder.
- Blade speed: The speed at which the blade spreads and levels the powder.
- Shell thickness: The thickness of the shell boundary that separates the core and shell areas of the printed part. Binder saturation in the shell was constant (dark body set to 8), while binder saturation in the core was varied based on the dark body factor levels. See [19] for a visual explanation.
- Binder saturation grade: The binder saturation is controlled by a technological parameter named "dark body" in the used machine. A dark body value of 8 corresponds to fully saturated pixels, whereas a value of 3 results in 69% pixel saturation, which means a lower binder saturation [20]. For a better understanding, following the term "binder saturation grade" will be used to refer to the technological parameters (dark body).

Table 2 provides the parameter configurations for the nine experiments. Other printing parameters were kept constant, including a layer thickness of 42 µm, an image resolution of 1200 DPI, and a bed temperature of 80 °C.

After printing the build box was heated to 200 °C for 8 h to dry the binder's aqueous component and crosslink its polymer component. Green samples were then carefully extracted during de-powdering for quality assessment.

A Hexagon DEA Global S 07-10-07 coordinate measuring machine (CMM) was used to measure the samples. The CMM, equipped with an HP-S-X1 probe, had a maximum permissible error (MPE) of 2.2 + L/300 µm, following ISO 10360–4 standards. A stylus with a 1 mm spherical tip was used for smaller geometries (Le10Li6, Le10Li8), while a 3 mm spherical tip was employed for larger geometries (Le20Li16, Le20Li18).

Samples were clamped to the CMM's working plane using a centering clamping system. The datum reference system, shown in Fig. 1, was defined in the following order:

- X–Z plane: was used to orient the first datum.
- Y–Z plane: was used to locate the second datum.
- X–Y plane: was used to block the third datum.

On each surface nine points were acquired, and planes were reconstructed using the least squares method. Since the bottom plane was inaccessible by probe tip, some points were acquired from the support to calculate the sample's height.

Sample dimensions were calculated based on the distances between planes, and dimensional accuracy was determined using Eq. (1), which compares measured dimensions (L_{Meas}) with nominal ones (L_{Nom}).

$$\text{Accuracy Index} = \frac{L_{\text{Meas}} - L_{\text{Nom}}}{L_{\text{Nom}}} \tag{1}$$

Geometrical accuracy was assessed by measuring flatness and parallelism errors. The flatness of all vertical planes was measured. While, as shown in Fig. 1, the parallelism of two external and four internal planes was evaluated with respect to the datum reference system. A naming convention was adopted for clarity, where "P," "E," and "I" indicate Plane, External, and Internal, respectively. XYZ indicates the printing reference system, with *plus* and *minus* subscripts representing plane orientations relative to the reference system.

In preliminary work, a statistical analysis was performed to identify the set of parameters that minimize dimensional deviation in each direction. The results showed that the optimal printing parameters vary depending on printing directions [21]. For this reason, a multi-objective optimization approach was adopted to find the process conditions that globally minimize dimensional deviation across all dimensions and across all four geometries. To simultaneously optimize dimensional and geometrical accuracy across all four geometries, a grey relational analysis (GRA) was performed, following the procedure in [22, 23]. A "smaller-the-better" approach was used to minimize response variables. Accuracy index (y_{ij}) was normalized using Eq. (2).

$$x_{ij} = \frac{\max(y_{ij}) - y_{ij}}{\max(y_{ij}) - \min(y_{ij})} \tag{2}$$

where:

- x_{ij} represents the normalized value of response parameter y_{ij},

Table 2 Matrix of the experiment and factor's levels according to Taguchi model

Experiment n°	Printhead Speed [mm/s]	Binder Saturation grade [-]	Blade Speed [mm/s]	Shell Thickness [pixel]
1	150	0	25	1
2	150	3	30	2
3	150	6	38	5
4	200	0	30	5
5	200	3	38	1
6	200	6	25	2
7	250	0	38	2
8	250	3	25	5
9	250	6	30	1

- The subscript i represents the experiment number, which ranges from 1 to 9.
- The subscript j corresponds to the response variable, which ranges from 1 to 20. This includes five accuracy indices (LX-EXT, LY-EXT, LZ, LX-INT, LY-INT) for each of the four geometries (Le10Li6, Le10Li8, Le20Li16, Le20Li18).
- *min* and *max* refer to the minimum and maximum values of the response parameter across the nine experiments, considering each geometry separately.

The deviation sequence (Δ_{ij}) was calculated using Eq. (3), representing the absolute difference between the reference ($x_{0j} = 1$) and the normalized response parameter (x_{ij}).

$$\Delta_{ij} = \|x_{0j} - x_{ij}\| \tag{3}$$

Grey relational coefficient (ξ_{ij}) was computed using Eq. (4), where $\Delta_{\min}$ and $\Delta_{\max}$ correspond to the minimum and maximum values of the deviation sequences. The distinguishing coefficient (ζ) was set to 0.5.

$$\xi_{ij} = \frac{\Delta_{\min} + \zeta\,\Delta_{\max}}{\Delta_{ij} + \zeta\,\Delta_{\max}} \tag{4}$$

Grey relational grades (γ_i) were then computed by using Eq. (5).

$$\gamma_i = \sum_{j=1}^{n} \omega_j \xi_{ij} \tag{5}$$

where ω_j is the weight factor associated with the different response variables. In this study no weight factor was adopted since all response variables were considered equally important.

Finally, the mean grey relational grade (Mean GRG) was computed using Eq. (6), averaging grey relational grades (γ_i) values for each factor level to identify the most influential factors and optimal printing configuration.

$$Mean\,GRG_{ji} = \frac{1}{n}\sum_{i}^{n}(\gamma_{ji}) \tag{6}$$

3 Results and discussion

3.1 Dimensional accuracy

Figure 2 illustrates the accuracy of external linear dimensions (LX-EXT, LY-EXT, LZ) across the experiments. The results are presented using boxplots, which display the range from the 25th to the 75th percentile of the sampled data. Within the rectangular box, the bold line represents the median value, while the whiskers extend to the maximum and minimum values. Dots outside the whiskers indicate outliers, which are values exceeding 1.5 times the interquartile range.

Despite variations due to printing conditions, external features generally exhibit positive deviations from the nominal dimensions. This finding aligns with literature summarized in Table 3. As listed in the table, many literature works have investigated dimensional deviation by using simple cubic shapes of 10 mm square. Generally, the deviation is positive or close to zero. The results of this work showed a maximum average deviation of 0.46%, which is significantly less in comparison to other studies. The reason is attributed to the higher performance of industrial printers in comparison to the laboratory systems.

Figure 3 depicted the accuracy of internal dimensions that generally show negative deviations. Such results, according to the best of the authors' knowledge, have not been reported in literature.

The observed positive deviations of external features and negative deviations of internal features are attributed to the interaction between the powder and binder. Essentially, when

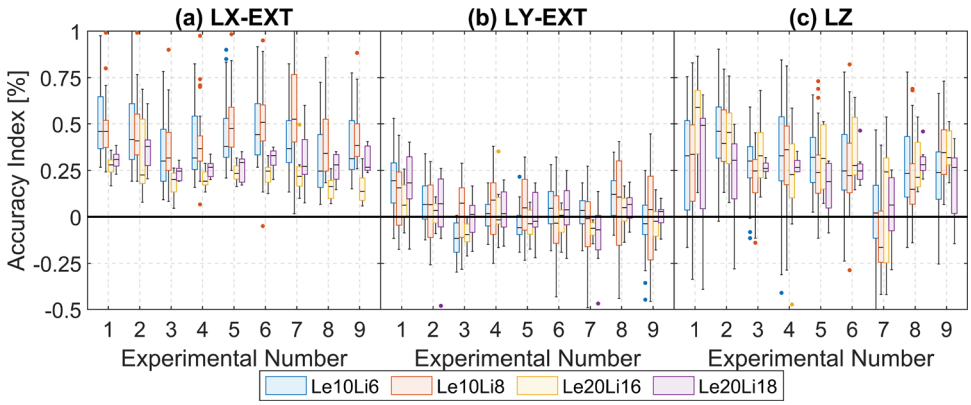

Fig. 2 Accuracy index of external linear dimensions as function of experiments. (**a**) LX-Ext dimension. (**b**) LY-Ext dimension. (**c**) LZ dimension

binder is deposited, it penetrates vertically and laterally into the voids between particles [25, 30]. This vertical and lateral permeation can result in the bonding of extra powder, leading to larger external dimensions and smaller internal dimensions. Jiang et al. studied dimensional accuracy by varying binder saturation from 50 to 140%. Their analysis showed a slight increase in dimensional deviation as binder saturation increased, which became more significant when bleeding defects occurred [28]. Similar results were found by Du et al. in [32]. Additionally, Cheny et al. observed that increasing drying time reduced dimensional deviation along both powder spreading and building directions [26].

In this study, the accuracy of LY-EXT is slightly positive and occasionally centered around zero. It is likely that binder penetration is more effective or extensive in the binder injection direction compared to the opposite direction, resulting in differential accuracy.

Further analysis of Figs. 2 and 3 reveals higher accuracy and precision along powder spreading direction (Y). Accuracy is slightly higher along building direction (Z) than binder spreading direction (X), but higher precision is observed in the X than in the Z direction. This is attributed to higher in-plane resolution (1200 DPI) compared to the layer resolution of 42 μm. Similar findings of the highest accuracy along powder spreading direction have been reported in other studies of 316L [25, 26]. However, as reported in Table 3, these results are not consistent across studies. Some works found the highest accuracy along building direction [24, 27, 29–31]. This is likely due to the complex behavior of powder-binder interaction. Future studies should investigate how this interaction is affected by particle size, powder material, binder properties, and printing conditions to develop a solid model for predicting and controlling dimensional accuracy.

As demonstrated in Figs. 2 and 3, accuracy appears to be influenced by geometry. For instance, the accuracy index for LX-EXT and LX-INT decreases as linear dimensions increase. This trend seems to be due to a virtually constant error in manufacturing. The powder-binder interaction is likely the primary factor affecting accuracy; however, other aspects may also contribute to dimensional deviation. It is worth mentioning the printing resolution. Essentially, the printer performs a geometry conversion based on image resolution (DPI) and layer thickness. Blunk et Seibel experimentally verified a building limit for length and diameter smaller than 0.1 mm using a DMP2500, the updated version of the DMP2000 printer. Below this limit, features were either not printed or deviated significantly from nominal size. They explained that larger measured dimensions result from geometry conversion, where the nominal dimension is converted to an equivalent number of pixels. If the conversion provides a fractional number of pixels, Blunk et Seibel stated that machine tends to round to the nearest larger integer [33].

In conclusion, this analysis highlights the role of printing directions, sample geometry, and printer resolution in determining dimensional accuracy. Further studies should explore the physical and technological causes of dimensional deviation loss in more detail.

3.2 Geometrical accuracy

Figure 4 shows the flatness form error for the external vertical planes as a function of the nine experiments. The data is presented using a box plot, following the same scheme as reported in Fig. 2.

Flatness form error is virtually constant across the nine experiments. The value ranges from 0.01 to 0.03, which is much lower compared to the results reported in [11, 34]. No significant differences are observed as a function of printing direction or sample geometry. The error is of the same order of magnitude as the particle distribution, which is D10 8.1 μm D50 15.3 μm, D90 27 μm, according to the powder supplier. The D50 size is comparable to the median flatness form error in the different batches. Therefore, the flatness form error seems to be attributed to surface irregularities, which can be induced during printing and de-powdering. Slight variations in the binder saturation, and dry conditions can result in more or fewer particle attached to the surface, as suggested by [3].

Table 3 Literature review of dimensional accuracy of linear dimensions in the green state categorized by printer, material, nominal geometry, and building directions (binder injection, powder spreading, and building direction)

Reference	Printer	Material	Nominal geometry [mm]	binder injection direction [%]	powder spreading direction [%]	building direction [%]
Present study	DMP2000	316L	Le10Li6	0.42 ± 0.20	0.03 ± 0.14	0.28 ± 0.26
			Le10Li8	0.46 ± 0.19	0.03 ± 0.21	0.24 ± 0.28
			Le20Li16	0.23 ± 0.14	− 0.01 ± 0.10	0.32 ± 0.26
			Le20Li18	0.29 ± 0.08	− 0.01 ± 0.10	0.14 ± 0.46
[24]	self-developed printer	316L	Cuboids 10 × 10x10	0.71 ± 0.20	2.33 ± 0.28	− 0.06 ± 0.85
[25]	ExOne Innovent +	316L – coarse powder	Prismatic samples 15 × 8x6 and 35 × 5x5	8.1 ± 0.3	3.3 ± 0.5	14.1 ± 0.5
		316L – coarse–fine powder ratio 9:1		3.3 ± 0.2	1.9 ± 0.2	4.2 ± 0.3
		316L – coarse–fine powder ratio 9:1		3.2 ± 0.1	1.9 ± 0.4	3.8 ± 0.4
[26]	ExOne Innovent + Equipped with Triple ACT	316L	Cuboids 10 × 10x10	/	0.90 ± 0.39	1.41 ± 0.55
[27]	ExOne Innovent	CoCrMo powder	Cuboids 10 × 10x10	1.1 ± 1.2	1.2 ± 0.05	0.44 ± 0.54
	ExOne Innovent +			0.29 ± 0.07	0.96 ± 0.07	0.40 ± 0.45
[28]	ExOne Innovent	Inconel 625 –water atomized	Cuboids 10 × 10x10	/	1.5	/
		Inconel 625 – argon atomized		/	1.3	/
[29]	ExOne Innovent +	Inconel 625	Cuboids 17.25 × 17.25x17.39	3.37	0.95	0.83
[30]	ExOne M-lab system	Ti6Al4V	Cuboids 8 × 8x8	0.75	0.5	0.0
[31][1]	ExOne Innovent	Copper	Cuboids 11 × 11x11	2.3	1.5	0.6
			Shell Cuboids 11 × 11x11	2.5	1.5	0.6
			Cylinder 10 × 10	1.3	1.3	0.8

[1]Data derived from the figure, not numerically reported in the paper

Additionally, some powders may not be completely removed during the de-powdering, causing geometrical error.

Figures 5 and 6 show the parallelism error for planes X and Y, respectively, obtained from the nine experiments.

Similarly to flatness, no significant differences were found when comparing the two-printing directions, X (binder injection) and Y (powder spreading), or when comparing external and internal planes. Despite slight variability across the experiments, the geometrical error can be attributed to the surface irregularities caused by the powder-binder interaction and de-powdering, as discussed in the flatness section.

There is a lack of experimental data in the literature for comparison. In another study, Zago et al. measured a parallelism error of 0.106 mm between planes parallel to the printing plane [11]. The significant difference can be attributed to variations in sample geometry, printer, and plane orientation. Generally, flatness and parallelism errors seem negligible when compared to defects caused by improper

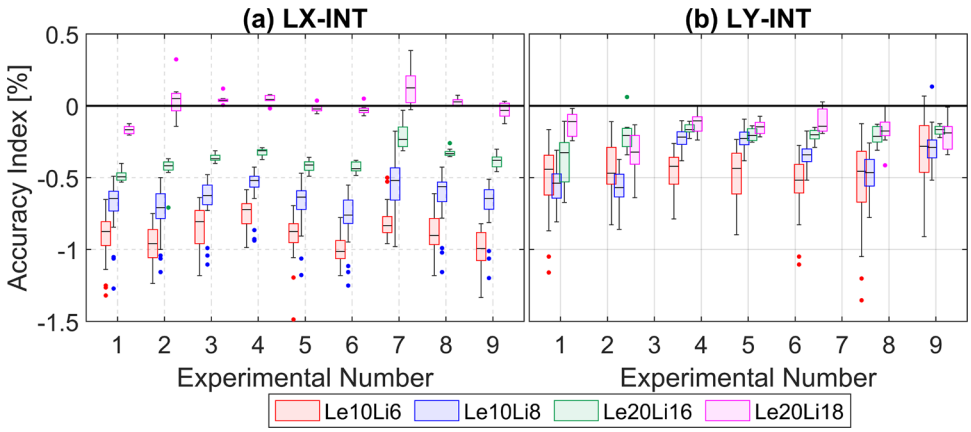

Fig. 3 Accuracy index of internal linear dimensions as function of experiments. (**a**) LX-INT dimension. (**b**) LY-INT dimension

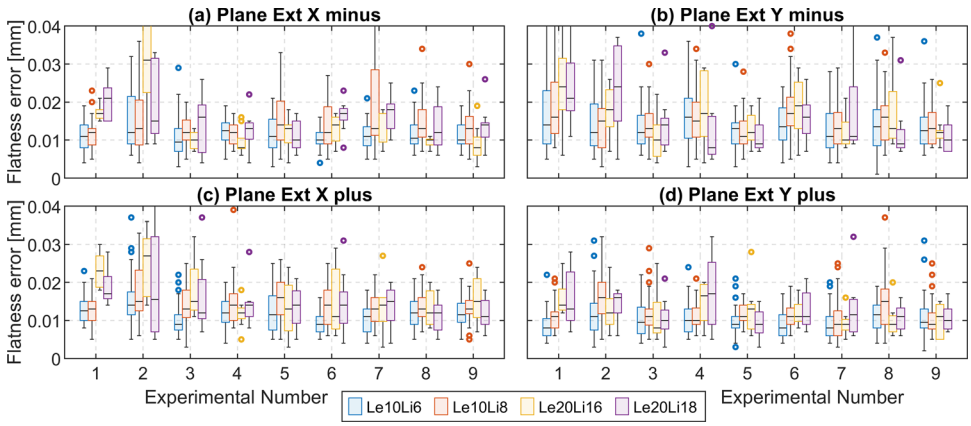

Fig. 4 Flatness form error as a function of experiments and sample geometries. (**a**) Plane X-Ext-minus – datum A plane, (**b**) Plane Y-Ext-minus – datum B plane, (**c**) Plane X-Ext-plus, (**d**) plane Y-Ext-plus

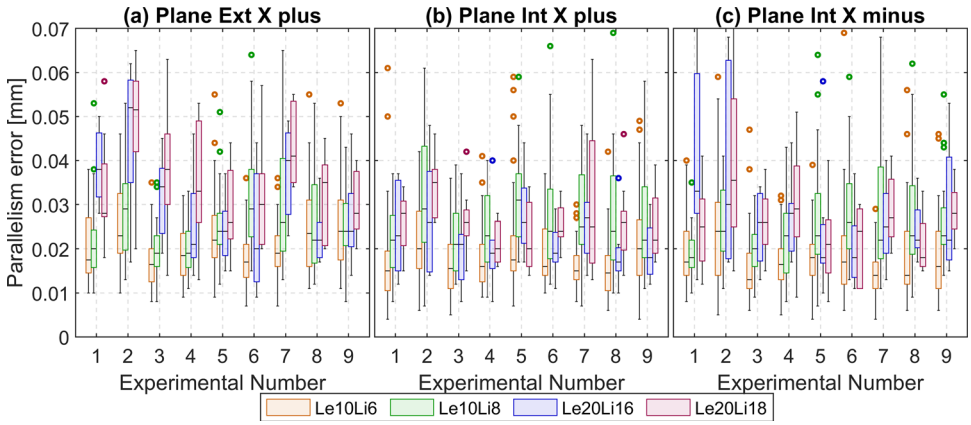

Fig. 5 Parallelism error of planes X (binder injection direction) as a function of experiments. (**a**) Plane Ext X-plus, (**b**) plane Int X-plus, (**c**) plane Int X-minus

printing conditions, as reported by Miyanaji et al. in [35]. The results of this work appear to be related to the limitations of this technology.

Differently by flatness analysis, parallelism error seems to be affected by sample geometry. In most cases, parallelism error increases as the height-to-thickness ratio increases. This error is likely related to layer-shifting caused by the compaction force applied by the blade. Some studies have examined the effect of compaction force applied by blade or roller. Maximenko et al. numerically modelled shape distortion induced by blade on part printed in the previously deposited layer [36]. Cao et al. modelled the stress field induced during powder leveling and correlated it with experimental layer-shifting and geometrical errors caused by changes in the printing process and powder leveling method [34]. Further analysis is needed to clarify the origin of the geometrical error to address possible solutions.

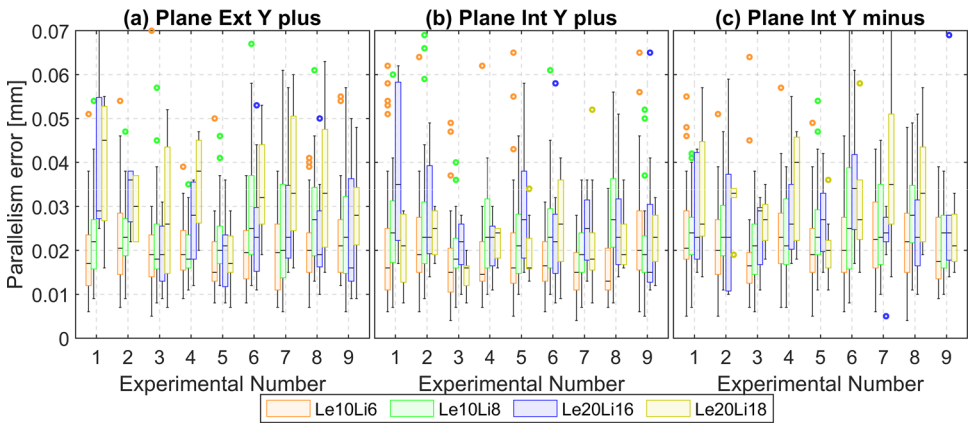

Fig. 6 Parallelism error of planes Y (powder spreading direction) as a function of experiments. (**a**) Plane Ext Y-plus, (**b**) plane Int Y-plus, (**c**) plane Int Y-minus

Table 4 Grey relational coefficients (GRC) distinguished for four geometry and the all sampling

Experiment n°	Grey relational coefficient [-]	Rank
1	0.532	7
2	0.552	5
3	0.586	3
4	0.495	9
5	0.507	8
6	0.550	6
7	0.598	2
8	0.566	4
9	0.618	1

3.3 Grey relational analysis

The average values of the accuracy index for the five dimensions investigated (LX-EXT, LY-EXT, LZ, LX-INT, LY-INT) across the four geometries in the nine experiments are reported in the appendix. This data was used to determine the optimal printing parameters that minimize deviation from nominal geometry. Flatness and parallelism errors were not considered, since they showed no significant variations as a function of printing parameters.

Grey relational analysis was employed to determine optimal printing parameters that minimize accuracy index across all samples. Grey relational coefficients were computed following the procedure outlined in the methodology section. The results are presented in Table 4, which includes all four geometries (all-sampling). Experiment 9 provided the highest grey relational coefficient, and the lowest rank was assigned to it. This means that experiment 9 provided the optimal printing parameters to minimize dimensional deviation among the nine experiments. The parameters combination is A3, B3, C2, D1, which means the higher level of printhead speed (A3) and binder saturation grade (B3), the intermediate level of blade speed (D2), and the lowest level of shell thickness (D1).

Table 5 reports the mean grey relational grade for each factor level. The difference between the maximum and minimum values shows that printhead speed is the most relevant printing parameter, followed by binder saturation grade, shell thickness and blade speed.

Figure 7 presents the means of grey relational grades. As observed in Table 5, greater variation in mean GRG indicates that the factor is more sensitive to the dimensional accuracy. Additionally, higher means of GRG correspond to the better responses. Consequently, according to Fig. 7, the optimal printing parameters are A3, B3, C3, D2, which correspond to level 3 of printhead speed, level 3 of binder saturation grade, level 3 of blade speed, and level 2 of shell thickness. This parameter combination slightly changes in comparison to the rank analysis reported in Table 4, meaning that the optimal process set-up, based on the means of grey relational grades analysis, was not included in the nine experiments.

Table 6 presents the analysis of variance (ANOVA) for grey relational grades. Since blade speed has the least significant effect, it was pooled out and considered as a residual error. The data reveals that printhead speed is a statistically significant factor affecting dimensional accuracy, with a P-value less than 0.05. Binder saturation grade has a P-value slightly greater than 0.05, suggesting it is not statistically significant at the 5% significant threshold. It is worth mentioning that an interaction between powder spreading and binder saturation grade may not be captured by fractional factorial analysis. This can be observed by analyzing the parameter levels of the three experiments with the highest rankings in Table 4. Experiments 9 and 7, ranked first and second respectively, have the most significant parameter at level 3, while experiment 3, ranked third, combines the lowest printhead speed with level 3 of the binder saturation grade. Given that the Taguchi L9 model consists of only nine experimental runs, the resulting low statistical power increases the risk of Type II errors—meaning that some real factor effects may go undetected. Therefore, further studies with larger sample sizes are needed to confirm the findings of this work.

Table 5 Response table based on grey relational grades

Level	Factor			
	Printhead speed (A)	Binder Saturation Grade (B)	Blade Speed (C)	Shell Thickness (D)
1	0.557	0.542	0.550	0.552
2	0.517	0.542	0.555	0.567
3	0.594	0.585	0.564	0.549
Max – Min	0.077	0.043	0.014	0.018
Rank	1	2	4	3

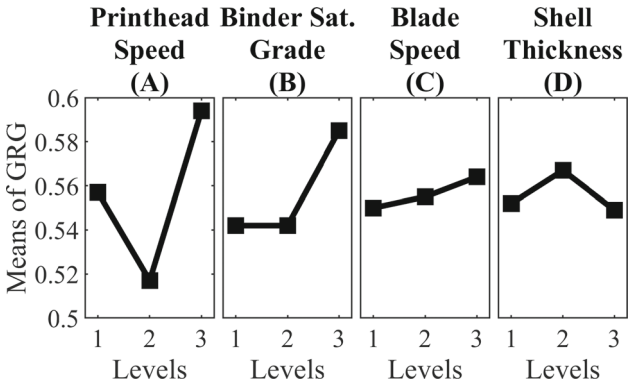

Fig. 7 Effect of process levels on means of grey relational grades. (**a**) Printhead speed, (**b**) binder saturation grade, (**c**) blade speed, (**d**) shell thickness

The optimal printing levels for parameters B, C, and D may be selected differently from those values indicated by the analysis of the mean of the grey relational grades, as their variations are not significant according to ANOVA. Based to the literature [19], the density and bending strength in the green state are statistically affected by the binder saturation grade, with higher levels increasing these properties. Consequently, similarly to the GRG analysis results, the highest binder saturation grade can be selected to maximize the mechanical properties of the intermediate product for safe handling between printing and sintering operation.

Similarly, choosing the highest blade speed (C3) could represent the optimal production choice, as it reduces printing time. Alternatively, parameters B and C can be determined according to environmental considerations and manufacturing costs. Increasing the binder content theoretically raises both manufacturing costs and CO_2 emissions during the debinding process, due to binder decomposition. Therefore, the lowest binder saturation grade and shell thickness may yield significantly lower CO_2 emissions and reduced production costs.

Further studies will investigate the statistical impact of the binder saturation grade in a sustainability perspective, and future work will aim to quantify the trade-offs among mechanical properties, manufacturing costs, and the sustainable production of the intermediate green product.

3.4 Design guideline

This research highlights that dimensional deviation is influenced by both printing parameters and printing directions. Higher accuracy was found along the powder spreading printing direction, which should be considered when determining the part's orientation in the printing box. For the first time, it has been shown that internal features exhibit greater deviations from the nominal green geometry than external features. Moreover, deviation appears to be influenced by the nominal size of the product. Based on these findings, product accuracy could be improved by changing the process conditions and part geometry.

Regarding the process, an optimal combination of printing parameters was proposed to minimize the dimensional deviation across all the sampled dimensions. In the authors' opinion, this set of parameters could be reliably applied to 316L products within the same dimensional range investigated in this study. The results are not limited to squared samples, but also applicable to more complex products that

Table 6 Analysis of Variance for Signal-to-noise ratios

Source	Degree of Freedom	Seq SS	Adj SS	Adj. MS	F-value	P-value
Printhead speed	2	2.1812	2.1812	1.0906	33.18	0.029
Binder Saturation grade	2	0.9064	0.9064	0.4532	13.79	0.068
Blade speed	polled	\	\	\	\	\
Shell thickness	2	0.1457	0.1457	0.0728	2.22	0.311
Residual Error	2	0.0657	0.0657	0.0329		
total	8	3.2991				

combine multiple features. However, some limitations may arise for products with internal features that are not aligned with the building direction, as well as for cylindrical and free-form shapes. Moreover, this study investigated only four printing parameters; further research should explore other parameters that may affect part accuracy.

Regarding part geometry, green product geometries are typically created by scaling the nominal sintered geometry according to the expected anisotropic shrinkage during sintering. However, the results of this study indicate that scaling factors should also account for dimensional deviations introduced during the printing process. Specifically, different scaling factors may be needed not only for different printing directions but also for internal and external features. Future studies should aim to develop a scaling factor model as a function of nominal dimensions distinguishing external and internal dimensions.

In this study, flatness and parallelism were only minimally affected by the printing parameters, likely because the measured values are close to the technological limits of the printer. Reducing particle size of powder base material appears to be the most promising strategy to mitigate these geometric errors. Furthermore, parallelism error increases with the height-to-thickness ratio, likely due to the compaction force applied by the blade. Further investigation into powder spreading could help identify optimal procedures to minimize this error.

4 Conclusions

This study provides novel insights into the accuracy of green products printed using the binder jetting additive manufacturing technology. Specifically, the study aimed to assess the influence of printing parameters and geometry on product accuracy. An L9 Taguchi methodology was employed to study the influence of four factors (printhead speed, binder saturation grade, blade speed, and shell thickness) at three levels. Four geometries were measured in the green state using a coordinate measuring machine to evaluate dimensional and geometrical accuracy.

The main findings are as follows:

- Dimensional accuracy is significantly affected by the printing direction, feature size, and feature type. Accuracy was highest in the powder spreading direction (external dimensions: 0.12% ± 0.21%; internal dimensions: − 0.41% ± 0.23%), followed by the building direction (0.25% ± 0.3%) and the binder injection direction (external dimensions: 0.40% ± 0.2%; internal dimensions: − 0.66% ± 0.32%). In general, dimensional accuracy increases with feature size. Additionally, external features showed higher accuracy compared to internal features. These findings are primarily attributed to the powder-binder interaction. The binder permeates vertically and laterally out of the nominal contour causing the positive deviation of external features and the negative deviation of internal features. This effect is more pronounced along the binder injection and building directions, leading to differential accuracy across the 3D directions.
- Flatness form error remained relatively constant across the nine batches, ranging between 0.01 mm and 0.03 mm. This form error is attributed to extra powder attached to the nominal surface during printing or residual powder not completely removed during de-powdering.
- Parallelism error is influenced by printing parameters and sample geometry. As the height-to-thickness ratio increases, the error significantly rises, likely due to layer-shifting caused by the compaction force applied during the blade movement.
- A grey relational analysis was employed to simultaneously optimize printing parameters to minimize dimensional deviations. According to this analysis, printhead speed (A) was identified as the most critical parameter, followed by binder saturation grade (B), shell thickness (D), and blade speed (C). The optimal printing configuration, based on the means of grey relational grades analysis, is achieved using level 3 for printhead speed, binder saturation grade, and blade speed, while using level 2 for shell thickness: A3, B3, C3, D2.
- ANOVA analysis reveals that printhead speed is statistically significant on dimensional accuracy having a P-value lower than 0.05, while P-value is slightly higher (0.068) for binder saturation grade.

For the first time, this study systematically evaluated both dimensional and geometrical accuracies in green products printed via binder jetting, revealing that anisotropic dimensional accuracy does not necessarily correspond to differential geometrical accuracy across the three printing directions. Further research is recommended to explore the relationship between binder-powder interactions and dimensional deviation. In conclusion, some design guidelines were proposed for optimizing accuracy by acting on both product design and manufacturing setup.

Appendix

Tables 7, 8, 9 and 10 report the average values of accuracy index for the five dimensions investigated (LX-EXT, LY-EXT, LZ, LX-INT, LY-INT) across the four geometries in the nine experiments.

Table 7 Average values of accuracy index for different experiments – geometry Le10Li6

Le10Li6	Accuracy index				
Experiment n°	LX-EXT [%]	LY-EXT [%]	LX-INT [%]	LY-INT [%]	LZ [%]
1	0.526	0.188	− 0.903	− 0.521	0.308
2	0.470	0.078	− 0.988	− 0.455	0.473
3	0.345	− 0.119	− 0.848	− 0.452	0.305
4	0.391	0.014	− 0.753	− 0.485	0.330
5	0.451	− 0.037	− 0.901	− 0.546	0.306
6	0.493	0.051	− 1.018	− 0.538	0.290
7	0.412	0.022	− 0.811	− 0.319	0.007
8	0.317	0.104	− 0.884	− 0.809	0.262
9	0.391	− 0.038	− 1.007	− 0.728	0.236

Table 8 Average values of accuracy index for different experiments – geometry Le10Li8

Le10Li8	Accuracy index				
Experiment n°	LX-EXT [%]	LY-EXT [%]	LX-INT [%]	LY-INT [%]	LZ [%]
1	0.475	0.122	− 0.694	− 0.550	0.287
2	0.445	0.030	− 0.725	− 0.565	0.426
3	0.356	0.035	− 0.649	− 0.229	0.212
4	0.399	0.062	− 0.561	− 0.227	0.300
5	0.509	0.056	− 0.693	− 0.352	0.237
6	0.506	− 0.022	− 0.770	− 0.468	0.266
7	0.569	− 0.046	− 0.545	− 0.294	− 0.134
8	0.418	0.066	− 0.625	− 0.500	0.197
9	0.434	− 0.034	− 0.686	− 0.396	0.350

Table 9 Average values of accuracy index for different experiments – geometry Le20Li16

Le20Li16	Accuracy index				
Experiment n°	LX-EXT [%]	LY-EXT [%]	LX-INT [%]	LY-INT [%]	LZ [%]
1	0.273	0.082	− 0.485	− 0.390	0.510
2	0.385	0.022	− 0.446	− 0.198	0.424
3	0.176	− 0.091	− 0.364	− 0.162	0.347
4	0.206	0.034	− 0.325	− 0.201	0.194
5	0.238	− 0.035	− 0.417	− 0.207	0.395
6	0.231	− 0.023	− 0.431	− 0.209	0.355
7	0.235	− 0.071	− 0.206	− 0.169	0.075
8	0.158	0.032	− 0.326	− 0.264	0.279
9	0.156	− 0.028	− 0.384	− 0.247	0.349

Table 10 Average values of accuracy index for different experiments – geometry Le20Li18

Le20Li18	Accuracy Index				
Experiment n°	LX-EXT [%]	LY-EXT [%]	LX-INT [%]	LY-INT [%]	LZ [%]
1	0.307	0.189	− 0.167	− 0.131	0.150
2	0.364	0.033	0.046	− 0.328	0.017
3	0.237	− 0.003	0.045	− 0.117	0.265
4	0.260	0.036	0.045	− 0.149	0.060
5	0.261	0.008	− 0.019	− 0.114	0.160
6	0.310	0.034	− 0.028	− 0.176	0.262
7	0.313	− 0.098	0.136	− 0.201	0.039
8	0.272	0.047	0.027	− 0.223	0.298
9	0.306	0.004	− 0.035	− 0.171	0.006

Funding Open access funding provided by Università degli Studi di Trento within the CRUI-CARE Agreement. The project is financed by Provincia Autonoma di Trento, L.P. 13/12/1999, n. 6, Art. 5: Aiuti per la promozione della ricerca e sviluppo. The authors are grateful to the whole staff of Mimest s.r.l. for producing the samples and fruitfully cooperating.

Data availability Data sets generated during the current study are available from the corresponding author on reasonable request.

References

1. Srivastava, A.K., Kumar, A., Kumar, P., Gautam, P., Dogra, N.: Research Progress in metal additive manufacturing: challenges and opportunities. Int. J. Interact. Des. Manuf. (2023). https://doi.org/10.1007/s12008-023-01661-6
2. de Pastre, M.A., Quinsat, Y., Lartigue, C.: Effects of additive manufacturing processes on part defects and properties: a classification review. Int. J. Interact. Des. Manuf. **16**, 1471–1496 (2022). https://doi.org/10.1007/s12008-022-00839-8
3. Chen, H., Zhao, Y.F.: Process parameters optimization for improving surface quality and manufacturing accuracy of binder jetting additive manufacturing process. Rapid Prototyp. J. **22**, 527–538 (2016). https://doi.org/10.1108/RPJ-11-2014-0149
4. Miyanaji, H., Momenzadeh, N., Yang, L.: Effect of powder characteristics on parts fabricated via binder jetting process. Rapid Prototyping J. **25**, 332–342 (2019). https://doi.org/10.1108/RPJ-03-2018-0069
5. Lores, A., Azurmendi, N., Agote, I., Zuza, E.: A review on recent developments in binder jetting metal additive manufacturing: materials and process characteristics. Powder Metall. **62**, 267–296 (2019). https://doi.org/10.1080/00325899.2019.1669299
6. Wang, Y., Zhao, Y.F.: Investigation of sintering shrinkage in binder jetting additive manufacturing process. Procedia Manuf. **10**, 779–790 (2017). https://doi.org/10.1016/j.promfg.2017.07.077
7. Mao, Y., Cai, C., Zhang, J., Heng, Y., Feng, K., Cai, D., Wei, Q.: Effect of sintering temperature on binder jetting additively manufactured stainless steel 316L: densification, microstructure evolution and mechanical properties. J. Mater. Res. Technol. **22**, 2720–2735 (2023). https://doi.org/10.1016/j.jmrt.2022.12.096
8. Huber, D., Vogel, L., Fischer, A.: The effects of sintering temperature and hold time on densification, mechanical properties and microstructural characteristics of binder jet 3D printed 17–4 PH stainless steel. Addit. Manuf. **46**, 102114 (2021). https://doi.org/10.1016/j.addma.2021.102114
9. Arni, R., Gupta, S.K.: Manufacturability analysis of flatness tolerances in solid freeform fabrication. J. Mech. Des. **123**, 148–156 (2001). https://doi.org/10.1115/1.1326439
10. Paul, R., Anand, S.: Optimal part orientation in rapid manufacturing process for achieving geometric tolerances. J. Manuf. Syst. **30**, 214–222 (2011). https://doi.org/10.1016/j.jmsy.2011.07.010
11. Zago, M., Lecis, N., Mariani, M., Cristofolini, I.: Analysis of the flatness form error in binder jetting process as affected by the inclination angle. Metals (2022). https://doi.org/10.3390/met12030430
12. Zago, M., Lecis, N., Mariani, M., Uçak, O.U., Cristofolini, I.: Influence of shape distortion on the precision of holes in parts fabricated by metal binder jetting. Int. J. Interact. Des. Manuf. **18**, 5789–5800 (2024). https://doi.org/10.1007/s12008-023-01357-x
13. Miyanaji, H., Momenzadeh, N., Yang, L.: Effect of printing speed on quality of printed parts in binder jetting process. Addit. Manuf. **20**, 1–10 (2018). https://doi.org/10.1016/j.addma.2017.12.008
14. Crane, N.B.: Impact of part thickness and drying conditions on saturation limits in binder jet additive manufacturing. Addit. Manuf. **33**, 101127 (2020). https://doi.org/10.1016/j.addma.2020.101127
15. Huang, S.J., Ye, C.S., Zhao, H.P., Fan, Z.T.: Parameters optimization of binder jetting process using modified silicate as a binder. Mater. Manuf. Process. **35**, 214–220 (2020). https://doi.org/10.1080/10426914.2019.1675890
16. Bai, Y., Wagner, G., Williams, C.B.: Effect of particle size distribution on powder packing and sintering in binder jetting additive manufacturing of metals. J. Manuf. Sci. Eng. **139**, 1–15 (2017). https://doi.org/10.1115/1.4036640

17. Clayton, J., Millington-Smith, D., Armstrong, B.: The application of powder rheology in additive manufacturing. Jom. **67**, 544–548 (2015). https://doi.org/10.1007/s11837-015-1293-z
18. Zago, M., Lecis, N., Mariani, M., Cristofolini, I.: Analysis of the causes determining dimensional and geometrical errors in 316L and 17–4PH stainless steel parts fabricated by metal binder jetting. Int. J. Adv. Manuf. Technol. **132**, 835–851 (2024). https://doi.org/10.1007/s00170-024-13437-7
19. Zago, M., Segata, G., Perina, M., Molinari, A.: Binder jet 3D printing of 316L stainless steel: a Taguchi analysis of the dependence of density and mechanical properties on the printing parameters. J. Mater. Res. Technol. **34**, 337–347 (2025). https://doi.org/10.1016/j.jmrt.2024.12.052
20. Dahmen, T., Henriksen, N.G., Dahl, K.V., Lapina, A., Pedersen, D.B., Hattel, J.H., Christiansen, T.L., Somers, M.A.J.: Densification, microstructure, and mechanical properties of heat-treated MAR-M247 fabricated by binder jetting. Addit. Manuf. (2021). https://doi.org/10.1016/j.addma.2021.101912
21. Zago, M., Cristofolini, I.: Optimization of Printing Parameters Using Taguchi Method to Improve the Quality of Parts Produced by Metal Binder Jetting. In: Advances on Mechanics, Design Engineering and Manufacturing V, pp. 211–220 (2025). https://doi.org/10.1007/978-3-031-72829-7_17
22. Çaydaş, U., Hasçalik, A.: Use of the grey relational analysis to determine optimum laser cutting parameters with multi-performance characteristics. Opt. Laser Technol. **40**, 987–994 (2008). https://doi.org/10.1016/j.optlastec.2008.01.004
23. Babu, V.V.P., Kumar, G.B.V., Barmavatu, P.: Dimensional accuracy testing and analysis of 3D metal printed SS316l using DMLS technique. Int. J. Interact. Des. Manuf. **19**, 375–392 (2025). https://doi.org/10.1007/s12008-024-01824-z
24. Chen, L., Chen, W., Fu, Z., Ding, G., Chen, Z., Zhu, D.: Binder jet 3D printing of 316L stainless steel: orthogonal printing and sintering process optimization. Adv. Eng. Mater. **25**, 1–12 (2023). https://doi.org/10.1002/adem.202200641
25. Liang, X., Meng, X., Ni, P., Zhao, Z., Deng, X., Chen, G., Chen, Y., Li, S., Wu, S., Liu, J., Qu, Z., Jin, F.: Effect of feedstock bimodal powder mixture and infiltration process on mechanical behaviour of binder jetting processed 316L stainless steel. Powder Metall. **66**, 387–402 (2023). https://doi.org/10.1080/00325899.2023.2213005
26. Cheny, T., Colin, C., Verquin, B.: Experimental evaluation of binder infiltration depth and axial overlap to control properties of green parts produced by binder jetting. Addit. Manuf. **87**, 104231 (2024). https://doi.org/10.1016/j.addma.2024.104231
27. Dorula, M., Khademitab, M., Jamalkhani, M., Mostafaei, A.: Location dependency of green density and dimension variation in binder jetted parts. Int. J. Adv. Manuf. Technol. **132**, 2853–2861 (2024). https://doi.org/10.1007/s00170-024-13529-4
28. Jiang, R., Monteil, L., Kimes, K., Mostafaei, A., Chmielus, M.: Influence of powder type and binder saturation on binder jet 3D–printed and sintered Inconel 625 samples. Int. J. Adv. Manuf. Technol. **116**, 3827–3838 (2021). https://doi.org/10.1007/s00170-021-07496-3
29. Du, W., Hayes, J., Myers, K., Barua, B., Yu, W., Singh, D.: Development of a high-temperature Inconel 625 heat exchanger by model design and binder jetting additive manufacturing. Mater. Des. **251**, 113333 (2025). https://doi.org/10.1016/j.matdes.2024.113333
30. Miyanaji, H., Zhang, S., Yang, L.: A new physics-based model for equilibrium saturation determination in binder jetting additive manufacturing process. Int. J. Mach. Tools Manuf **124**, 1–11 (2018). https://doi.org/10.1016/j.ijmachtools.2017.09.001
31. Choong, Y.H., Krishnan, M., Gupta, M.: A printability evaluation of fine and coarse powder in binder jetting of dense and porous copper parts. Prog. Addit. Manuf. **8**, 1103–1125 (2023). https://doi.org/10.1007/s40964-022-00380-w
32. Mao, Y., Li, J., Li, W., Cai, D., Wei, Q.: Binder jetting additive manufacturing of 316L stainless-steel green parts with high strength and low binder content: binder preparation and process optimization. J. Mater. Process. Technol. **291**, 117020 (2021). https://doi.org/10.1016/j.jmatprotec.2020.117020
33. Blunk, H., Seibel, A.: Design guidelines for metal binder jetting. Prog. Addit. Manuf. **9**, 725–732 (2024). https://doi.org/10.1007/s40964-023-00475-y
34. Cao, S., Qiu, Y., Wei, X.F., Zhang, H.H.: Experimental and theoretical investigation on ultra-thin powder layering in three dimensional printing (3DP) by a novel double-smoothing mechanism. J. Mater. Process. Technol. **220**, 231–242 (2015). https://doi.org/10.1016/j.jmatprotec.2015.01.016
35. Miyanaji, H., Orth, M., Akbar, J.M., Yang, L.: Process development for green part printing using binder jetting additive manufacturing. Front. Mech. Eng. **13**, 504–512 (2018). https://doi.org/10.1007/s11465-018-0508-8
36. Maximenko, A.L., Olumor, I.D., Maidaniuk, A.P., Olevsky, E.A.: Modeling of effect of powder spreading on green body dimensional accuracy in additive manufacturing by binder jetting. Powder Technol. **385**, 60–68 (2021). https://doi.org/10.1016/j.powtec.2021.02.070